

Large and Robust Charge-to-Spin Conversion in Sputtered Weyl Semimetal WTe_x with Structural Disorder

Xiang Li^{1,2*}, Peng Li³, Vincent D.-H. Hou⁴, Mahendra DC¹, Chih-Hung Nien⁴, Fen Xue¹, Di Yi³,
Chong Bi², Chien-Min Lee⁴, Shy-Jay Lin⁴, Wilman Tsai⁴, Yuri Suzuki³, and Shan X. Wang^{1,2**}

¹Department of Materials Science and Engineering, Stanford University, Stanford, California
94305, USA

²Department of Electrical Engineering, Stanford University, Stanford, California 94305, USA

³Department of Applied Physics, Stanford University, Stanford, California 94305, USA

⁴Corporate Research, Taiwan Semiconductor Manufacturing Company, Hsinchu, Taiwan

Email address: *xiangli@stanford.edu, **sxwang@stanford.edu

Abstract:

Topological insulators have recently shown great promise for ultralow-power spin-orbit torque (SOT) devices thanks to their large charge-to-spin conversion efficiency originating from the spin-momentum-locked surface states. Weyl semimetals, on the other hand, may be more desirable due to their spin-polarized surface as well as bulk states, robustness against magnetic and structural disorder, and higher electrical conductivity for integration in metallic magnetic tunnel junctions. Here, we report that sputtered WTe_x thin films exhibit local atomic and chemical structures of Weyl semimetal WTe_2 and host massless Weyl fermions in the presence of structural disorder at low temperatures. Remarkably, we find superior spin Hall conductivity and charge-to-spin conversion efficiency in these sputtered WTe_x films compared with crystalline WTe_2 flakes. Besides, the strength of unidirectional spin Hall magnetoresistance in annealed $\text{WTe}_x/\text{Mo}/\text{CoFeB}$ heterostructure is up to 20 times larger than typical SOT/ferromagnet bilayers reported at room temperature. We further demonstrate room temperature field-free magnetization switching at a current density as low as 0.97 MA/cm^2 . These large charge-to-spin conversion properties that are robust in the presence of structural disorder and thermal annealing pave the way for industrial production of Weyl semimetals. Our results open up a new class of sputtered Weyl semimetals for memory and computing based on magnetic tunnel junctions as well as broader planar heterostructures containing SOT/ferromagnet interfaces.

Introduction

Recently, topological insulators (TIs) [1, 2] emerge as a promising class of materials for converting charge current to spin-polarized current. Owing to their strong spin-orbit coupling and spin-momentum locked surface states [3, 4], TIs promises larger charge-to-spin conversion efficiency (ξ_{ST}) than spin-transfer torque (STT) filtering through a ferromagnetic metal (FM) or spin-orbit torque (SOT) arising from a heavy metal (HM). However, bulk states that dominate electron conduction in some TIs such as Bi_2Se_3 might not convert charge to spin as efficiently as surface states.[5-8] Also, when interfacing TIs with ferromagnetic metal (FM) in a magnetic tunnel junction (MTJ) configuration, magnetic impurities diffused out of the FM layer may drive the TI into a trivial state,[9] while TI's helical surface states may be destroyed due to hybridization with metal bands,[10] making the TI/FM interface vulnerable to annealing or thermal effects. Lastly, for practical applications such as SOT-Magnetic Random Access Memory (MRAM), most of the current and power divert into the FM layer due to TIs' much higher resistivity ($> 1000 \mu\Omega \text{ cm}$)[5, 6, 11] than FM such as CoFeB ($\sim 130 \mu\Omega \text{ cm}$), while TIs also introduce large parasitic resistance in series with the MTJ. As the tunneling magnetoresistance of a MTJ is rather limited ($< 600\%$)[12], an insulating SOT write line would significantly degrade the MTJ readout signal, which precludes TIs' integration in future generations of MRAM.

In contrast, Weyl semimetals (WSMs),[13, 14] such as type-II WSM WTe_2 , shows great prospect to overcome the above challenges. Both the surface Fermi arcs and bulk Weyl nodes are spin-polarized in WTe_2 . [15-17] WSMs' Weyl nodes and spin-momentum-locked surface states persist under broken time reversal and inversion symmetries, and are immune to disorder-induced Anderson localization.[18, 19] Another advantage of using WSMs to generate SOT compared with TIs is their higher conductivity (σ_{xx}) arising from its semi-metallic band structure and high carrier mobility [20], resulting in smaller parasitic resistance and current shunted into the FM layer.

In the past few years, ξ_{ST} larger than one has been demonstrated in TI/FM heterostructures at room temperature [5, 6, 21, 22]. Lately, research also shows a large damping-like ξ_{ST} up to 0.5 in WTe_2 ,[23] low-temperature enhancement of field-like torque when a current flows along its b axis [24], as well as an out-of-plane damping-like ξ_{ST} around 0.013 when a

current flows along its a axis.[25] However, most of the spintronics studies using topological materials employ crystalline TIs grown by molecular beam epitaxy (MBE) [5, 6, 21, 22, 26] and exfoliated WSM flakes from bulk crystals [23-25], which are not suitable for large-scale industrial manufacturing. Therefore, it is highly desirable to use industrial deposition techniques, such as sputtering to grow these novel topological materials. Surprisingly, amorphous $\text{Bi}_x\text{Se}_{(1-x)}$ prepared by sputtering or thermal evaporation exhibits similar topological properties as crystalline TIs, such as high ξ_{ST} [11, 27] as well as surface states using angle-resolved photoemission spectroscopy[28]. Moreover, a recent theoretical work shows a topological metal phase in 3D amorphous metals exhibiting similar and even larger Hall conductivity over their crystalline counterparts.[29] However, no work has experimentally investigated the effect of structural disorder in topological semimetals.

Here, we report large and robust charge-to-spin conversion properties in sputtered disordered WSM WTe_x . We first confirm our sputtered WTe_x materials show similar local atomic and chemical structures as crystalline WTe_2 . Through low-temperature magnetoresistance and temperature-dependent resistance measurements, we find that WTe_x film hosts quasi-2D or 3D Weyl fermions depending on its thickness. The increase of structural disorder with WTe_x thickness also drives a crossover from weak anti-localization to weak localization. We characterize the SOT properties of as deposited $\text{WTe}_x/\text{CoFeB}$ bilayers using spin-torque ferromagnetic resonance (ST-FMR), showing large spin Hall conductivity up to $1 \times 10^5 (\hbar/2e) \Omega^{-1}m^{-1}$ and ξ_{ST} up to 0.8 at room temperature, which are larger than the corresponding values reported for crystalline WTe_2 flakes. We also find 5-20 times larger unidirectional spin Hall magnetoresistance (USMR) signal in thermally annealed $\text{WTe}_x/\text{Mo}/\text{CoFeB}$ heterostructure than existing FM/HM or FM/TI bilayers, possibly driven by magnon-scattering of spin-polarized Weyl fermions in WTe_x . We further demonstrate room-temperature field-free magnetization switching at a current density as low as 0.97 MA/cm^2 in this annealed heterostructure using a simple planar USMR device geometry.

Results

Material Properties of WTe_x Thin Films

We first confirm the sputtered WTe_x films share similar local chemical and atomic structures as crystalline WTe_2 via Raman spectroscopy and X-ray Photoelectron Spectroscopy (XPS). Raman spectroscopy is a widely used technique to identify materials based on their unique phonon vibrational mode fingerprints determined by crystal structure and chemical bonding. As shown in Figure 1a, we observe Raman modes B_1^{10} , A_2^4 , A_1^9 , A_1^6 , A_1^5 , A_1^2 in uncapped single layer WTe_x samples with different thicknesses (t_{WTe_x}). As t_{WTe_x} increases, A_1^5 and A_1^2 Raman modes show smaller widths, while the A_1^2 peak frequency decreases (Figure S1), which are consistent with the reports on bulk and flaked WTe_2 films.[30, 31]. We further employed XPS to confirm that the chemical bonding state of Te atoms in our WTe_x material is the same as that in WTe_2 . As shown in Figure 1b, the binding energy of Te 3d_{5/2} electron is consistent with WTe_2 state reported in exfoliated flakes (572.7 eV), compared with metallic Te (573.0 eV) and TeO_x (576.3 eV). [32, 33]

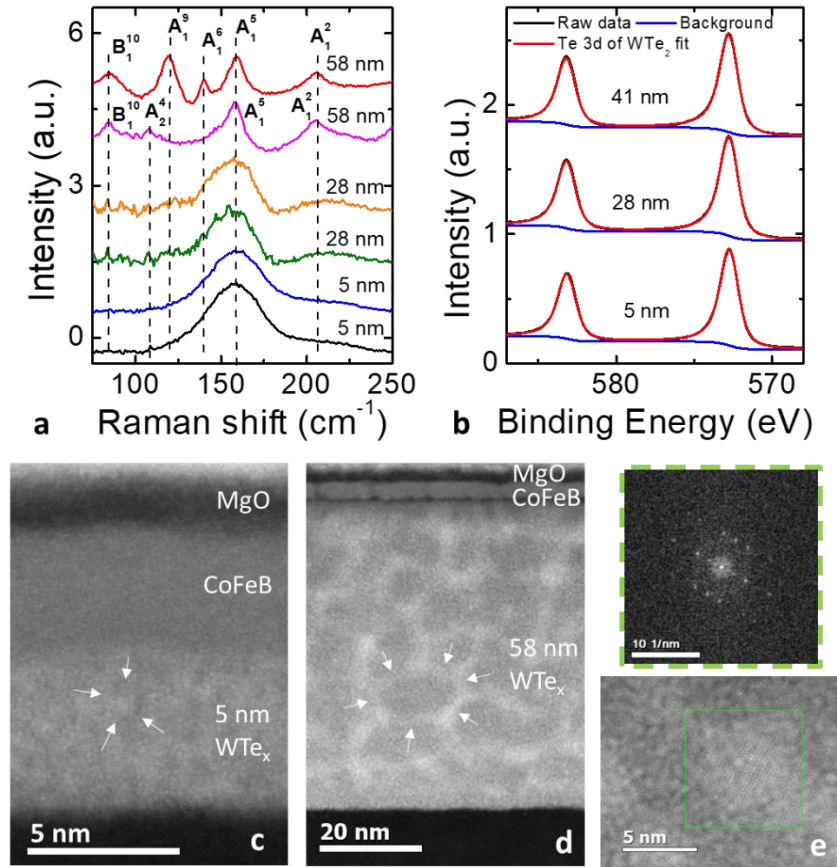


Figure 1. Material properties of WTe_x films with different thicknesses. a, Raman spectroscopy of uncapped WTe_x films with different thicknesses measured the same day when deposited. The

Raman vibrational modes are labeled. **b**, X-ray Photoelectron Spectroscopy (XPS) profile of Te 3d binding energy region for WTe_x films with different thicknesses, the data were obtained after *in situ* Ar ion sputtering of the capping layers on WTe_x films. A doublet of Te 3d_{5/2} and Te 3d_{3/2} peaks are separate by 10.4 eV. **c**, Cross-section scanning transmission electron microscopy (STEM) image of $\text{WTe}_x(5)/\text{CoFeB}(4)$ bilayer (hereafter, all numbers in parenthesis are in nm). **d**, Cross-section STEM image of $\text{WTe}_x(58)/\text{CoFeB}(4)$ bilayer. **e**, Cross-section STEM image of $\text{WTe}_x(47)/\text{CoFeB}(4)$ bilayer showing a small crystallite outlined by the green box. The digital diffractogram of the selected crystallite is shown in the green dashed box on top.

Then we study the evolution of structural disorder with the WTe_x films thickness based on Raman spectroscopy and atomic-scale structural and chemical characterizations. As shown in Figure 1a, two groups of Raman modes co-exist in our WTe_x films, i.e., a first group of $B_1^{10}, A_1^9, A_1^6, A_1^5, A_1^2$ modes and a second group of $B_1^{10}, A_2^4, A_1^5, A_1^2$ modes, which appear at different locations on the same 58 nm thick WTe_x sample (more data in Figure S1). As t_{WTe_x} decreases to 28 nm, modes in the two groups appear together accompanied with a mixture of A_1^6, A_1^5 modes. While for the 5 nm thick sample, only A_1^5, A_1^2 modes are visible, which is similar as reported in monolayer exfoliated WTe_2 flakes [30]. This first group appears when the laser is aligned along the *b* axis of bulk WTe_2 crystal, and the second group along the *c* axis.[30] The data suggest that as t_{WTe_x} increases, the WTe_x films segregate into small crystalline WTe_2 clusters with their *b* or *c* axis aligned normal. High-resolution bright-field scanning transmission electron microscopy (STEM) images on the 5 nm thick and 58 nm thick WTe_x films are shown in Figure 1c-d. We see the 5 nm thick WTe_x film exhibits an amorphous structure with sub-nm features, while in the 58 nm sample, ~10-nm features of dark clusters surrounded by white regions emerge. Using energy-dispersive X-ray spectroscopy (EDS), we find that the bright regions are W-rich with Te:W atomic ratio *x* down to 0.87, while the dark regions are Te-rich with *x* up to 1.49. The *x* ratio variation in the 58 nm sample appears to be slightly larger compared with the 47 nm WTe_x sample (Figure S2). Besides, we observe a small crystalline cluster embedded in amorphous WTe_x films, exhibiting diffraction patterns similar as crystalline WTe_2 [32, 34], as shown in Figure 1e. Taking together the Raman, STEM, and EDS data, we conclude that uniform amorphous films form when t_{WTe_x} is small (~ 5 nm), while segregation increases when t_{WTe_x} is greater. This increased

segregation may explain the two groups of Raman modes in 58 nm thick WTe_x.

Quantum Transport in Topological WTe_x Thin Films

To study the topological properties of the WTe_x thin films with different thickness thus segregation disorder, we measure magnetoresistance (MR) and temperature-dependent resistance. We find the increase of disorder and electron-phonon interaction drives a crossover from weak anti-localization (WAL) in a 2D Weyl fermion system (5 nm thick WTe_x), to weak localization (WL) in a 3D WSM system (41 nm thick WTe_x). As shown in Figure 2a, the 5 nm thick WTe_x film shows positive MR with a cusp-shaped perpendicular magnetic field (B_z) dependence at 4 K. We attribute this behavior to the WAL effect, which describes the destructive quantum interference of electron waves going around a self-intersecting path in opposite directions in a disordered electronic system with spin-orbit coupling (SOC).[35] This WAL behavior has been found in thin WTe₂ flakes [34, 36] and differs from reported classical quadratic MR [20, 36] and positive linear MR in WTe₂ [37, 38] (see Figure S3). In contrast, we find a negative MR in 41 nm thick WTe_x devices at 4 K, which we attribute to the WL effect driven by electron-phonon interaction. The almost identical negative MR when the magnetic field is aligned along different directions (see Figure S3) differs from chiral anomaly-induced negative MR which appears only when the magnetic field is parallel to the current.[39, 40].

We fit the 5 nm thick WTe_x MR curves using the simplified Hikami-Larkin-Nagaoka (HLN) equation describing the WAL correction to conductivity $\Delta\sigma_{xx} = \sigma_{xx}(B_z) - \sigma_{xx}(0)$ under perpendicular magnetic field B_z in a quasi-2D system with strong SOC [35]:

$$\Delta\sigma_{xx} \cong -\frac{\alpha_{HLN}e^2}{2\pi h} \left[\psi \left(\frac{1}{2} + \frac{B_\phi}{B_z} \right) - \ln \left(\frac{B_\phi}{B_z} \right) \right] \quad \text{Equation 1}$$

where ψ is the digamma function, B_ϕ is the phase coherence characteristic field, and α_{HLN} is 0.5 for WAL and -1 for WL. As shown in Figure 2c-d, the HLN equation yields a rather good fit up to ± 9 T and 50 K. The linear dependence of B_ϕ on temperature ($B_\phi \sim T^p, p = 1$) indicates that electron-electron interactions rather than electron-phonon interactions ($p = 3$) contribute to the dephasing of electron waves.[41] We confirm the quasi-2D nature of the 5 nm thick WTe_x as the effective dephasing length $l_\phi = \sqrt{\hbar/4eB_\phi}$ (ranging from 18 nm at 4 K to 5.2 nm at 50 K) is larger

than the WTe_x thickness. In contrast, fit based on a formula for the 3D system as proposed in [42] gives rise to l_ϕ and p values that are not consistent with the 3D system model. (see Figure S4). Meanwhile, a similar α_{HLN} decrease as temperature increases as well as similar α_{HLN} values between 0 and 0.5 have been observed in Dirac semimetal Cd_3As_2 films in the quasi-2D limit.[43] Moreover, as shown in Figure 2b, the change of sheet conductance $\Delta\sigma_{xx} = \sigma_{xx}(T) - \sigma_{xx}(4\text{K})$ as a function of temperature can be fitted up to 150 K using an equation describing 2D massless Dirac fermions [44], i.e., $\Delta\sigma_{xx} = (c_{ee} - c_{qi})\ln(T)$, where c_{ee}, c_{qi} describe the contributions from electron-electron interaction and quantum interference, respectively. Note that as inversion symmetry is broken in the 5 nm thick amorphous WTe_x , a Dirac node separates into two Weyl nodes.[14] Hence, the 5 nm thick WTe_x behaves as a quasi-2D massless Weyl fermion system with electron-electron interaction [45].

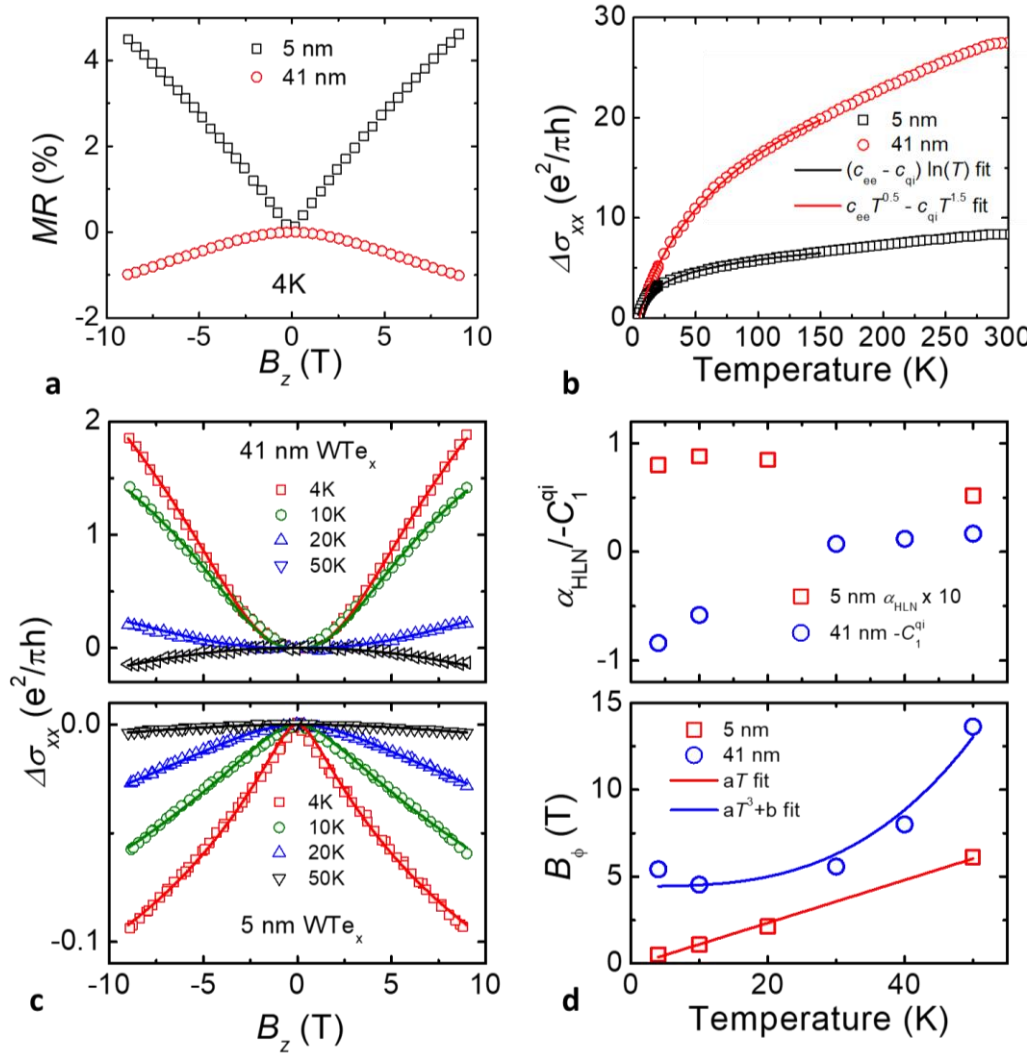


Figure 2. Temperature-dependent resistance measurements of WTe_x films with different thicknesses. **a**, Sheet resistance dependence on perpendicular magnetic field (B_z) for WTe_x capped with MgO/Ta, measured at 4K. **b**, Change in sheet conductance ($\Delta\sigma_{xx}$) dependence on temperature. The 5 nm and 41 nm data below 150 K are fitted using $(c_{ee} - c_{qi})\ln(T)$ and $c_{ee}T^{0.5} - c_{qi}T^{1.5}$ equations, respectively. **c**, Change in sheet conductance ($\Delta\sigma_{xx}$) dependence on B_z , measured at 4, 10, 20, and 50 K. The 5 nm and 41 nm data are fitted based on the 2D Hikami-Larkin-Nagaoka equation [35] and 3D WL/WAL formula proposed in [42], respectively. **d**, Dependence of phase coherence characteristic field (B_ϕ) and fit parameters ($\alpha_{HLN}, -C_1^{qi}$) on temperature. The B_ϕ values for 5 nm and 41 nm data are fitted using aT and aT^3+b functions, respectively.

In order to understand the mechanisms driving the crossover from WAL to WL as t_{WTe_x} increases to 41 nm,[44] we fit the change in sheet conductance $\Delta\sigma_{xx}$ as a function of B_z using an equation describing WL and WAL in 3D WSM as proposed in [42]:

$$\Delta\sigma_{xx} = \frac{c_1^{qi} B_z^2 \sqrt{B_z}}{B_\phi^2 + B_z^2} + \frac{c_2^{qi} B_\phi^2 B_z^2}{B_\phi^2 + B_z^2} \quad \text{Equation 2}$$

where fitting parameters C_1^{qi}, C_2^{qi} are positive for WL and negative for WAL. As shown in Figure 2**c-d**, the B_ϕ dependence on temperature can be fitted by a $aT^3 + b$ formula, indicating electron-phonon interaction ($B_\phi \sim T^p, p = 3$) is the dominating dephasing process, rather than electron-electron interaction ($p = 3/2$).[41] The non-zero B_ϕ value at 0 K indicates surface scattering and/or impurity also play a role in the 58 nm thick WTe_x film.[43, 46] Next, we fit the temperature dependence of $\Delta\sigma_{xx}$ up to 150 K using an equation [44] describing 3D Weyl fermions, $\Delta\sigma_{xx} = c_{ee}T^{0.5} - c_{qi}T^{p/2}$. The good fit using $p = 3$ further confirms the dominant role of electron-phonon interaction. We also verify that the 3D equation is valid as l_ϕ values of 3.5 to 6.0 nm are much smaller than the WTe_x thickness (41 nm), while a fit using the equation for the 2D massless Dirac fermions fails (see Figure S5). Therefore, the 41 nm thick WTe_x thin film is a 3D WSM and the segregation discussed above possibly leads to the strong electron-phonon interaction.

Charge-to-Spin Conversion in WTe_x/CoFeB Bilayers

We measure large charge-to-spin-conversion efficiency (ξ_{ST}) up to 0.8 in as-deposited WTe_x/CoFeB bilayers with varying t_{WTe_x} using the spin-torque ferromagnetic resonance (ST-FMR) technique. As illustrated in Figure 3a, by flowing GHz RF current through the WTe_x/CoFeB bilayers, the oscillating CoFeB anisotropic magnetoresistance driven by damping-like and field-like torques (τ_{DL}, τ_{FL}) generates a DC voltage when mixed with the RF current. Based on established methodology (Supplementary Note S6)[47], we fit the mixing voltage V_{mix} using symmetric and asymmetric Lorentzian shapes which originate from τ_{DL} and τ_{FL} respectively as in Figure 3b. The extracted ξ_{ST} values for different WTe_x thickness samples are shown in Figure 3c, where each ξ_{ST} value was averaged across 5, 6, 7, and 8 GHz measurements. Notably, the 58 nm thick WTe_x sample shows a large ξ_{ST} value up to 0.8 along with significant variations among different devices on the same sample, as shown in the inset of Figure 3c. This variation is consistent with the two groups of Raman modes due to strong segregation discussed above. An *ab initio* study on WTe₂ has also shown that the intrinsic spin Hall conductivity varies when current flows along different axes of WTe₂. [48]

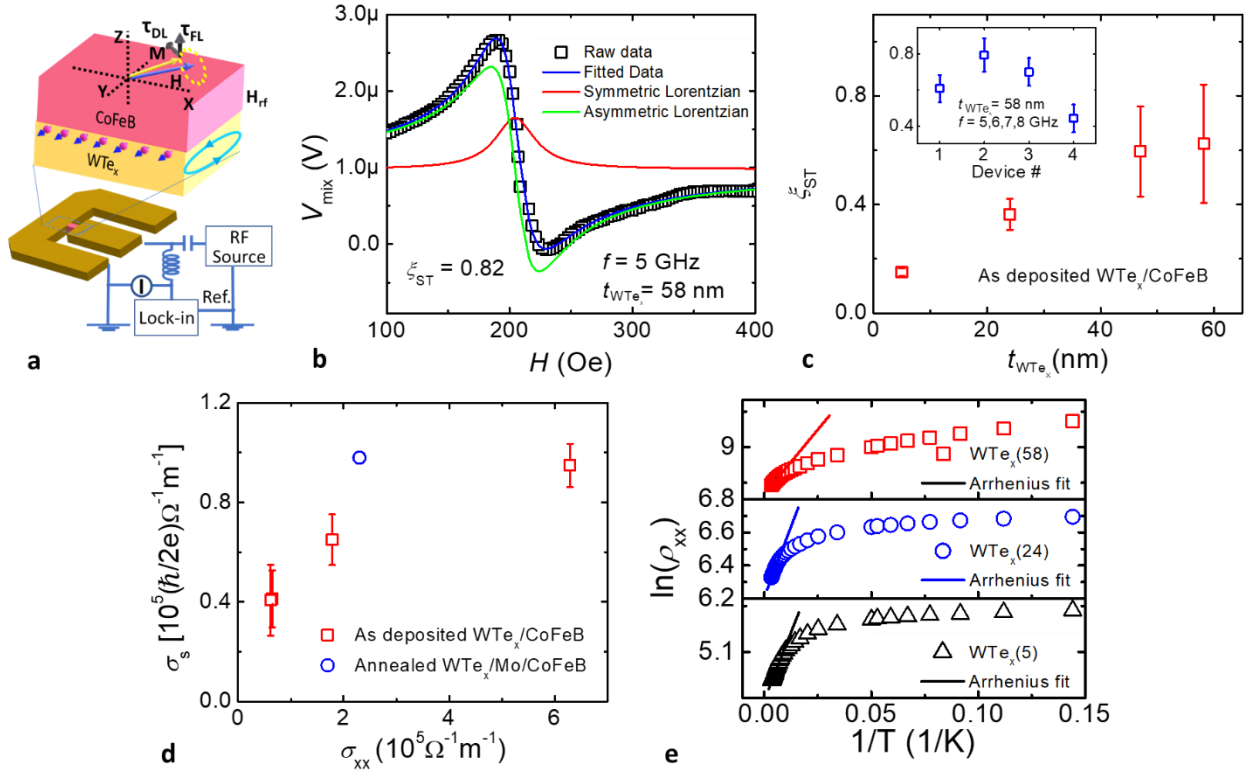


Figure 3. Charge-to-spin conversion in WTe_x/CoFeB bilayers with different WTe_x thicknesses. **a**, Schematic of spin-torque ferromagnetic resonance (ST-FMR) experimental setup using fabricated WTe_x(t_{WTe_x})/CoFeB(4)/MgO(2)/Ta(2) microstrips. The damping-like and field-like torques are labeled as τ_{DL} , τ_{FL} respectively. **b**, Representative mixing voltage obtained in ST-FMR measurement as a function of applied magnetic field H strength for WTe_x thickness of 58nm measured at 5 GHz RF excitation. The raw data is being fitted by a sum of symmetric and asymmetric Lorentzian. **c**, ξ_{ST} dependence on WTe_x thickness from ST-FMR measurements. Inset shows the charge-to-spin conversion efficiency ξ_{ST} for different devices on the 58nm-thick WTe_x sample, each data point are averaged from ST-FMR measurements at 5, 6, 7, and 8 GHz. **d**, WTe_x spin Hall conductivity σ_s as a function of longitudinal conductivity σ_{xx} for both as-deposited WTe_x/CoFeB and annealed WTe_x/Mo/CoFeB heterostructures, measured at room temperature. The t_{WTe_x} for the as-deposited data decreases from 58 nm to 5 nm from the left to the right. **e**, Resistivity of WTe_x single layer extracted from WTe_x/CoFeB bilayers resistivity as a function of inverse of temperature ($1/T$). The data from 150 to 300 K are fitted using Arrhenius equation $\rho = \rho_0 \exp(E_a/k_B T)$.

The monotonic increase in ξ_{ST} as a function of t_{WTe_x} , as shown in Figure 3c, suggests that bulk spin Hall contributions dominate the charge-to-spin conversion. This bulk origin is consistent with the observation of bulk Weyl fermions in WTe_x films at low temperatures. We further clarify the origins of the SHE through the evolution of spin Hall conductivity $\sigma_s (= \xi_{ST}/\rho_{xx})$ as a function of conductivity σ_{xx} , as shown in Figure 3d. The σ_{xx} is derived from a parallel resistor model (Supplementary Note S7). According to several theoretical and experimental studies on the SHE in metals [49, 50] and anomalous Hall effects in ferromagnets[51], a crossover from intrinsic metallic regime to dirty metal regime happens when σ_{xx} decreases to $10^5 - 10^6 \Omega^{-1}m^{-1}$ (ρ_{xx} increases to $100 - 1000 \mu\Omega cm$). In the intrinsic metallic regime, σ_s is roughly independent of σ_{xx} , while in the dirty metal regime, σ_s decreases rapidly as σ_{xx} decreases. Figure 3d indicates that σ_s increases with σ_{xx} (when WTe_x is relatively thick) and then flattens out at $\sigma_{xx} > 2 \times 10^5 \Omega^{-1}m^{-1}$ range (when WTe_x is relatively thin), which matches the reported crossover very well, suggesting that the increasing segregation disorder as t_{WTe_x} increases drives WTe_x towards the dirty metal regime. Notably, the 58 nm thick WTe_x film with strong segregation is not in the regime

of strong or Anderson localization (see Figure S8), confirming that Weyl semimetals are essentially immune to disorder-induced Anderson localization as predicted by theory.[52]

We further confirm this transition from intrinsic metal to dirty metal regime as t_{WTe_x} increases based on temperature-dependent resistivity measurements. As shown in Figure 3e, the insulating behavior is consistent with thermal activation-driven electron transport in the dirty metal regime.[51] Fitting of the resistivity data from 150 K to 300 K using a thermal activation model $\rho = \rho_0 \exp(E_a/k_B T)$ reveals increasing thermal activation energy E_a as t_{WTe_x} increases (Supplementary Note S7), which is consistent with our previous finding of increasing degree of segregation disorder as t_{WTe_x} increases. Research has shown similar insulating behavior in degraded crystalline WTe_2 flakes after exposure to air, consisting of 10×10 WTe_2 atoms crystalline clusters embedded in an amorphous matrix, [34] which we also observe in Figure 1e. Note that although we have observed insulating temperature-dependent behavior in our WTe_x materials, they are still gapless semimetals in the presence of localization because carriers are still present at the Fermi energy as evidenced by the WAL and WL behaviors at low temperature.[36]

In the context of SHE, both intrinsic and side-jump mechanisms contribute to the SHE in the intrinsic metallic regime. *Ab initio* theory [48] has calculated σ_s to be up to $0.5 \times 10^5 (\hbar/2e) \Omega^{-1} m^{-1}$ in WTe_2 due to intrinsic contributions, which is almost half of the σ_s value for our 5 nm thick WTe_x film ($0.95 \times 10^5 (\hbar/2e) \Omega^{-1} m^{-1}$). While the highest σ_s demonstrated in WTe_2 flakes reaches $0.88 \times 10^5 (\hbar/2e) \Omega^{-1} m^{-1}$ in exfoliated 120 nm thick WTe_2 flakes.[23] Hence, there is likely contributions from both intrinsic spin Hall effect and side-jump in our 5 nm thick WTe_x film. As side-jump contribution is proportional to impurity concentration, [53] it might play a significant role in our sputtered WTe_x films with structural disorder.

SOT-Induced Switching of WTe_x /Mo/CoFeB Heterostructures Detected via USMR

To demonstrate SOT-driven magnetization switching, we synthesized heterostructures composed of 5 nm thick WTe_x films with low resistivity and large σ_s , which is better matched with metallic CoFeB and has higher write efficiency. Integration of sputtered WTe_x films into CMOS backend processes calls for a stack design sustaining SOT properties after thermal annealing processes. Here, we insert 1-2 nm thick Mo between WTe_x and CoFeB due to the

excellent thermal annealing stability, while the low ξ_{ST} and large spin diffusion length of Mo will not significantly alter the SOT properties of the heterostructure. [54, 55] We first confirm there is no significant degradation of the WTe_x film's Raman spectrum after insertion of Mo and after 300 °C annealing (see Figure S9 and S10). Then we utilize second-harmonic Hall measurements to quantify the damping-like SOT in annealed WTe_x(5)/Mo(1)/CoFeB(1) heterostructure. Following established analysis methodology, [26, 56, 57] we determine that there are minimal field-like torque, Oersted field, thermoelectric effects (including anomalous Nernst and spin Seebeck effects), and damping-like SOT from the Mo insertion layer. We also obtain $\xi_{ST}^{WTe_x} = 0.426 \pm 0.004$, $\rho_{WTe_x} = 435 \mu\Omega \text{ cm}$, and σ_s of $0.98 \times 10^5 (\hbar/2e) \Omega^{-1} m^{-1}$ in this WTe_x(5)/Mo(1)/CoFeB(1) heterostructure, which is consistent with that of $0.95 \times 10^5 (\hbar/2e) \Omega^{-1} m^{-1}$ in as deposited WTe_x(5)/CoFeB(4) bilayer discussed in the last section. This confirms that high σ_s is sustained after insertion of Mo layer and thermal annealing. (Supplementary Note S11 and Figure S12)

We next characterize the unidirectional spin Hall magnetoresistance (USMR) effect which can distinguish magnetization along y and $-y$ directions via second-harmonic longitudinal resistance ($R_{2\omega}^{xx}$) measurements [58]. We use 300 °C-annealed WTe_x(5)/Mo(2)/CoFeB(1) heterostructures here for magnetization switching experiments as the CoFeB layer in the WTe_x(5)/Mo(1)/CoFeB(1) heterostructure has a negligibly small in-plane coercivity (see Figure S13). As shown in Figure 4a, when the magnetization aligns along different transverse orientations (y -axis), $R_{2\omega}^{xx}$ signal switches with a coercivity around 1-2 Oe. The $R_{2\omega}^{xx}$ signal vanishes at a large H_y field, as shown in Figure 4a inset, which we attribute to spin-dependent electron scattering between SOT spin current and magnons in the ferromagnet [59-62], rather than spin-dependent electron scattering between SOT spin currents and the magnetization [58, 61, 63]. We also determine the thermoelectric contribution to the USMR effect to be negligible (Supplementary Note S14). Following reference [59], we use total USMR per current density per total longitudinal resistance $\Delta R_{2\omega}^{xx}/J R_{xx}$ to benchmark the strength of USMR across various material stacks and device geometries. Here, $\Delta R_{2\omega}^{xx}$ is defined as the maximal change of USMR when magnetization points to $-y$ or y direction. Notably, the $\Delta R_{2\omega}^{xx}/J_{WTe_x} R_{xx}$ value of 82.2 ppm MA⁻¹cm² in this work is about 5-20 times higher than that in existing FM/HM or FM/TI bilayers (see Table S1). As the 5 nm thick WTe_x film hosts quasi-2D Weyl fermions at

low temperature, the large USMR strength suggests that highly spin-polarized Weyl fermions plays a critical role in converting charge to spin more efficiently than other HMs or TIs.

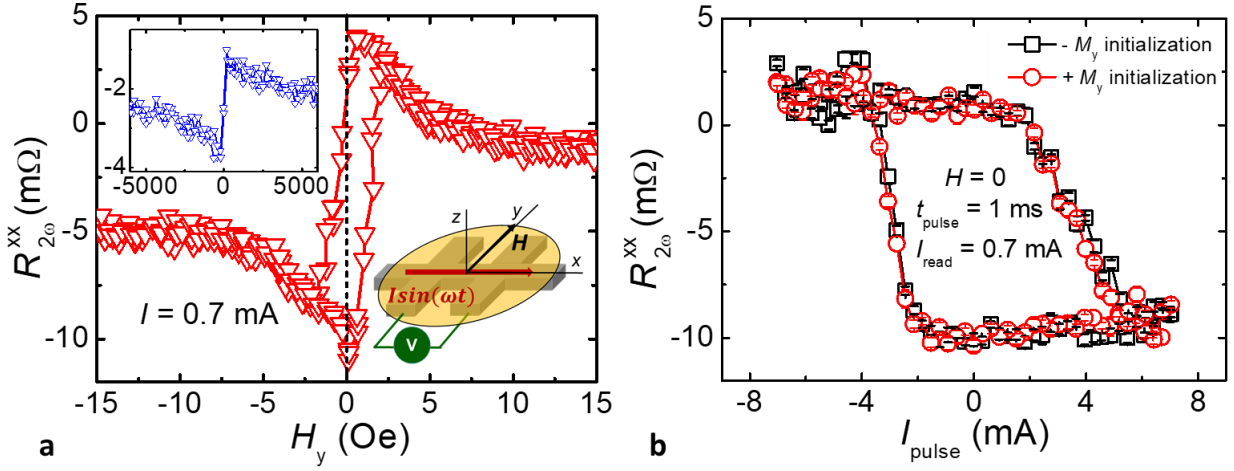


Figure 4. Pulsed SOT-induced switching in $\text{WTe}_x/\text{Mo}/\text{CoFeB}$ -based heterostructure detected via the USMR effect. **a**, Second-harmonic longitudinal resistance ($R_{2\omega}^{xx}$) as a function of the in-plane magnetic field along the y-axis (H_y) under an AC current amplitude of $I = 0.7\text{mA}$ for $\text{WTe}_x(5)/\text{Mo}(2)/\text{CoFeB}(1)/\text{MgO}(2)/\text{Ta}(2)$ heterostructure annealed at 300°C for 30 minutes. The dotted line corresponds to $H_y = 0$. The top-left inset shows $R_{2\omega}^{xx}$ under a wider range of H_y from -6000 Oe to 6000 Oe. The bottom-right inset shows the schematic of the second harmonic measurement with an input of sinusoidal current $I\sin(\omega t)$. **b**, $R_{2\omega}^{xx}$ measured as a function of pulse current amplitude I_{pulse} under zero external field. The current pulse width is 1 ms . The read current amplitude is 0.7 mA . The red and black curves correspond to initialization of magnetization along $-M_y$ and M_y direction respectively.

We then demonstrate room temperature pulsed current-driven switching of in-plane magnetization detected via the USMR effect and deduce a $\xi_{\text{ST}}^{\text{WTe}_x}$ value that is consistent with previous second-harmonic Hall measurements. First a square-shaped current pulse with a pulse width of t_{pulse} flows through the current channel, and subsequently the $R_{2\omega}^{xx}$ was measured under an AC read current. Similar magnetization switching curves at zero external magnetic field with opposite magnetization initialization directions as shown in Figure 4b confirms that current-

induced SOT drives the switching. The damping-like SOT from the WTe_x layer has an opposite sign to that of Pt [47] (Supplementary Note S15). The analog and gradual switching process indicates that multi-domains form during the switching process due to the small coercivity (< 2 Oe) of the CoFeB layer [64]. While the asymmetric switching current can be attributed to a small remnant field around 0.5 Oe during measurements, as seen from the shift of maximum and minimum $R_{2\omega}^{xx}$ values away from 0 field in Figure 4a. Note that 30.1% of the total current flows through the WTe_x layer based on a parallel resistor model. (see Figure S12) The lowest switching current density J_{WTe_x} achieved is 0.97 and 2.05 MA/cm² using a 100 ms pulse width.

Discussion

In contrast to the traditional method of detecting in-plane magnetization direction using a MTJ with two in-plane magnetic layers sandwiching a tunnel barrier, the USMR effect used in this work can detect in-plane magnetization switching in a simple planar WSM/FM bilayer geometry.[58] The 5-20 times larger USMR strength in our heterostructure not only shows promise of USMR-based novel bilayer spintronics devices, but also calls for more studies into the role of Dirac electrons/Weyl fermions-magnon scattering in charge-to-spin conversion physics.[59]

We last compare the charge-to-spin conversion properties in sputtered WTe_x films with single crystalline WTe₂ flakes and other SOT materials. Remarkably, the σ_s of 0.95 – 0.98 [$\times 10^5 (\hbar/2e) \Omega^{-1}m^{-1}$] in 5 nm thick sputtered WTe_x films exceeds that of $0.88 \times 10^5 (\hbar/2e) \Omega^{-1}m^{-1}$ in exfoliated 120 nm thick WTe₂ flakes.[23] Moreover, a large ξ_{ST} value up to 0.8 is achieved in 58 nm thick sputtered WTe_x films compared with around 0.2 for WTe₂ flakes at a similar thickness of 60 nm, as well as 0.51 in 120 nm thick WTe₂ flakes. The σ_s in 5 nm thick WTe_x is comparable with σ_s in the range of 0.4 – 2 [$\times 10^5 (\hbar/2e) \Omega^{-1}m^{-1}$] in MBE-grown Bi₂Se₃ and sputtered Bi_xSe_{1-x}, though the latter have resistivity values (1755 – 13000 $\mu\Omega cm$) much higher than the sputtered WTe_x (159 – 435 $\mu\Omega cm$). Our results are also comparable with sputtered narrow-bandgap TI Bi_{1-x}Sb_x with σ_s of 0.4 – 1.2 [$\times 10^5 (\hbar/2e) \Omega^{-1}m^{-1}$] and resistivity of 330 – 1000 $\mu\Omega cm$.[65] As the switching power in future SOT-MRAM designs is proportional to $\rho_{SOT}t_{SOT}/\xi_{ST}^2$, the sputtered WTe_x films promise up to 20 times lower write

power than WTe_2 flakes, as well as 15% and 2 times lower write power than W and Pt films, respectively (Supplementary Note S16). Our results will stimulate condensed matter theory and experimental studies to go beyond granular and amorphous TIs [11, 28, 66, 67], and to investigate the new class of topological amorphous or disordered semimetals [29] that are robust against time-reversal and inversion symmetry breaking as well as strong localization effects.

Methods

Material deposition

The WTe_x and Mo films were deposited using ion-beam sputtering techniques using a stoichiometric WTe_2 target and Mo target. The ion-beam sputtering was conducted using Xe gas under 0.1 mTorr at room temperature. Meanwhile, MgO, Ta, and $\text{Co}_{20}\text{Fe}_{60}\text{B}_{20}$ magnetron sputtering guns are also integrated into the same vacuum chamber. Hence, we can achieve *in-situ* growth of the whole stack discussed in the main text without breaking vacuum. The Ta and $\text{Co}_{20}\text{Fe}_{60}\text{B}_{20}$ layers were deposited using DC sputtering, while the MgO layers were deposited using RF sputtering from an insulating MgO target. The stacks with Mo insertion were annealed at 300 °C for 30 minutes using an All-Win Rapid Thermal Process (RTP) system with Ar ambient.

Device fabrication

Temperature-dependent magnetoresistance and resistance data were gathered from Hall bars patterned on $\text{MgO}(2)/\text{WTe}_x(5)/\text{MgO}(2)/\text{Ta}(2)$ and $\text{WTe}_x(58)/\text{Ta}(2)$ stacks using a four-point probe method. The $\text{WTe}_x/\text{CoFeB}(4.4)/\text{MgO}(2)/\text{Ta}(2)$ (number in parenthesis is in nm) stacks for ST-FMR measurements were fabricated into $10\ \mu\text{m} \times 40\ \mu\text{m}$ microstrips using standard photolithography and Ar ion mill techniques. The $\text{MgO}(2)/\text{WTe}_x(5)/\text{Mo}(1\text{ or }2)/\text{CoFeB}(1)/\text{MgO}(2)/\text{Ta}(2)$ (number in parenthesis is in nm) stacks for second harmonic measurements were fabricated into $10\ \mu\text{m} \times 130\ \mu\text{m}$ Hall bars using standard photolithography and Ar ion mill techniques. The patterned devices are subsequently covered with $\text{Ti}(5\text{ nm})/\text{Au}(120\text{ nm})$ as contacts using photolithography and liftoff techniques.

Film characterization

Raman spectroscopy: The Raman spectrum was gathered using a Horiba Labram HR Evolution Raman System with a laser of 532 nm wavelength, a grating of 600 l/mm, and objective magnification of 100x. Each spectrum is an average of 10 captures each collected over 10 s. The laser spot size is around 0.3 μm .

X-Ray Photoelectron Spectroscopy (XPS): The XPS spectrum was gathered using a PHI VersaProbe System with Al (K α) radiation (1486 eV). The focused ion gun used for *in situ* depth profiling has a sputter rate of around 2 nm/min with a beam energy of 500V 0.6 μA , and a raster size of 1 $\mu\text{m} \times 1 \mu\text{m}$.

Transmission Electron Microscopy (TEM) and Energy Dispersive X-ray Spectroscopy (EDS): Cross-sectional TEM samples were prepared with Focused Ion Beam technique (Thermo-Fisher Helios 460G4). At the final sample thinning stages, Ga ion beam energy was reduced from 30kV to 8kV, 2kV, and then 500V to mitigate ion damages over TEM lamella surfaces. TEM lamellas were imaged with Thermo-Fisher Metrios TEM equipped with probe Cs-correctors operated at 200kV. STEM high-angle annular dark-field (HAADF) imaging is the primary imaging mode used in this study, and the resolution is better than 0.13nm. EDS experiment was carried out in STEM mode with the probe current set to about 600pA. The EDS detector system is of SDD type with a nominal collection solid angle of 0.7 or 0.9 radians (Super-XTM or Dual-XTM, respectively). EDS data analysis was performed in Bruker's Esprit EDS software. Quantification of W:Te ratio in WTe_x film was obtained by using the built-in Cliff Lorimer factors of the Esprit EDS software. W signal maps (intensity of W M-lines) were processed by Principle Component Analysis (PCA) to isolate W-M lines from Si K-line and Ta-M lines.

Device Electrical Measurements

Spin-Torque Ferromagnetic Resonance (ST-FMR): ST-FMR measurements were performed on WTe_x/CoFeB microstrips with sizes of 60 x 40 μm^2 using the setup. The external H field is oriented with a ϕ angle of 45° with respect to the microstrip thus current flow direction. A GHz signal was generated by an HP 83640B microwave source and was sent through the WTe_x/CoFeB bilayer through a T-Bias and ground-signal-ground coplanar waveguide.

Second harmonic and pulsed switching measurements: The second harmonic setup consists of a Keithley 6221 current source providing AC current with a frequency of 1.333 kHz, and two Stanford Research SR830 Lock-in amplifiers recording the first and second harmonic signal of

longitudinal or Hall resistance of the Hall bar device. The pulse current used in the switching experiments were generated by Keithley 6221 through the square wave settings. The DC device resistance was obtained using a four-point probe method with Keithley 6221 current source and Keithley 2000 voltage meter.

Acknowledgments

This research was supported in part by ASCENT, one of six centers in JUMP, a Semiconductor Research Corporation (SRC) program sponsored by DARPA. Part of this work was performed at the Stanford Nano Shared Facilities (SNSF)/Stanford Nanofabrication Facility (SNF), supported by the National Science Foundation under award ECCS-1542152. The Stanford authors wish to thank NSF Center for Energy Efficient Electronics Science (E3S) and TSMC for additional financial support. The authors would also like to acknowledge Dan Ralph, Jian-Ping Wang, David Goldhaber-Gordon, Carlos H. Diaz, Donkoun Lee, Chris Hinkle, Ilan Rosen, Arturas Vailionis, Marcin Walkiewicz, and Andrey Malkovskiy for fruitful discussions.

Author contributions

X.L. conceived and designed the research with contributions from P.L., M.D., C.B., S.-J.L., W.T., Y.S., and S.X.W.. S.X.W. supervised the study. X.L. deposited the thin films, carried out Raman spectroscopy, XPS, and second harmonic measurements. X.L. and P.L. fabricated the Hall bar and microstrip devices and carried out ST-FMR measurements. X.L., P.L., and D.Y. carried out the SQUID measurements. V.H., C.-H.N., and C.-M.L. carried out TEM and EDS studies. X.L. performed data analysis with contributions from P.L., V.H., M.D., F.X., C.-H.N., S.-J.L., W.T., Y.S., and S.X.W. X.L. wrote and revised the manuscript with input and comments from all authors.

Additional information

Supplementary information is available in the online version of the paper. Correspondence and requests for materials should be addressed to X.L. and S.X.W.

Competing financial interests:

The authors declare no competing financial interests.

References

- [1] M. Z. Hasan and C. L. Kane, "Colloquium: Topological insulators," *Reviews of Modern Physics*, vol. 82, pp. 3045-3067, 11/08/ 2010.
- [2] X.-L. Qi and S.-C. Zhang, "Topological insulators and superconductors," *Reviews of Modern Physics*, vol. 83, pp. 1057-1110, 10/14/ 2011.
- [3] D. Hsieh, Y. Xia, D. Qian, L. Wray, J. H. Dil, F. Meier, *et al.*, "A tunable topological insulator in the spin helical Dirac transport regime," *Nature*, vol. 460, p. 1101, 07/20/online 2009.
- [4] C. H. Li, O. M. J. van 't Erve, J. T. Robinson, Y. Liu, L. Li, and B. T. Jonker, "Electrical detection of charge-current-induced spin polarization due to spin-momentum locking in Bi₂Se₃," *Nature Nanotechnology*, vol. 9, p. 218, 02/23/online 2014.
- [5] A. R. Mellnik, J. S. Lee, A. Richardella, J. L. Grab, P. J. Mintun, M. H. Fischer, *et al.*, "Spin-transfer torque generated by a topological insulator," *Nature*, vol. 511, pp. 449-51, Jul 24 2014.
- [6] Y. Wang, D. P. Zhu, Y. Wu, Y. M. Yang, J. W. Yu, R. Ramaswamy, *et al.*, "Room temperature magnetization switching in topological insulator-ferromagnet heterostructures by spin-orbit torques," *Nature Communications*, vol. 8, Nov 8 2017.
- [7] H. Wang, J. Kally, J. S. Lee, T. Liu, H. Chang, D. R. Hickey, *et al.*, "Surface-State-Dominated Spin-Charge Current Conversion in Topological-Insulator--Ferromagnetic-Insulator Heterostructures," *Physical Review Letters*, vol. 117, p. 076601, 08/11/ 2016.
- [8] Z. Jiang, C.-Z. Chang, M. R. Masir, C. Tang, Y. Xu, J. S. Moodera, *et al.*, "Enhanced spin Seebeck effect signal due to spin-momentum locked topological surface states," *Nature Communications*, vol. 7, p. 11458, 2016/05/04 2016.
- [9] M. Liu, J. Zhang, C.-Z. Chang, Z. Zhang, X. Feng, K. Li, *et al.*, "Crossover between Weak Antilocalization and Weak Localization in a Magnetically Doped Topological Insulator," *Physical Review Letters*, vol. 108, p. 036805, 01/19/ 2012.
- [10] J. Zhang, J. P. Velev, X. Dang, and E. Y. Tsymlal, "Band structure and spin texture of Bi_2Se_3 3d ferromagnetic metal interface," *Physical Review B*, vol. 94, p. 014435, 07/27/ 2016.
- [11] M. Dc, R. Grassi, J. Y. Chen, M. Jamali, D. Reifsnnyder Hickey, D. Zhang, *et al.*, "Room-temperature high spin-orbit torque due to quantum confinement in sputtered Bi₂Se₃(1-x) films," *Nat Mater*, vol. 17, pp. 800-807, Sep 2018.
- [12] S. Ikeda, J. Hayakawa, Y. Ashizawa, Y. M. Lee, K. Miura, H. Hasegawa, *et al.*, "Tunnel magnetoresistance of 604% at 300K by suppression of Ta diffusion in CoFeB / MgO / CoFeB pseudo-spin-valves annealed at high temperature," *Applied Physics Letters*, vol. 93, p. 082508, 2008.
- [13] X. Wan, A. M. Turner, A. Vishwanath, and S. Y. Savrasov, "Topological semimetal and Fermi-arc surface states in the electronic structure of pyrochlore iridates," *Physical Review B*, vol. 83, p. 205101, 05/02/ 2011.
- [14] A. A. Soluyanov, D. Gresch, Z. Wang, Q. Wu, M. Troyer, X. Dai, *et al.*, "Type-II Weyl semimetals," *Nature*, vol. 527, p. 495, 11/25/online 2015.
- [15] Y. Wu, D. Mou, N. H. Jo, K. Sun, L. Huang, S. L. Bud'ko, *et al.*, "Observation of Fermi arcs in the type-II Weyl semimetal candidate WTe_2 ," *Physical Review B*, vol. 94, p. 121113, 09/14/ 2016.
- [16] B. J. Feng, Y. H. Chan, Y. Feng, R. Y. Liu, M. Y. Chou, K. Kuroda, *et al.*, "Spin texture in type-II Weyl semimetal WTe_2 ," *Physical Review B*, vol. 94, Nov 18 2016.
- [17] J. Jiang, F. Tang, X. C. Pan, H. M. Liu, X. H. Niu, Y. X. Wang, *et al.*, "Signature of Strong Spin-Orbital Coupling in the Large Nonsaturating Magnetoresistance Material WTe_2 ," *Physical Review Letters*, vol. 115, p. 166601, 10/12/ 2015.

- [18] A. A. Zyuzin, S. Wu, and A. A. Burkov, "Weyl semimetal with broken time reversal and inversion symmetries," *Physical Review B*, vol. 85, p. 165110, 04/06/ 2012.
- [19] C.-Z. Chen, J. Song, H. Jiang, Q.-f. Sun, Z. Wang, and X. C. Xie, "Disorder and Metal-Insulator Transitions in Weyl Semimetals," *Physical Review Letters*, vol. 115, p. 246603, 12/11/ 2015.
- [20] M. N. Ali, J. Xiong, S. Flynn, J. Tao, Q. D. Gibson, L. M. Schoop, *et al.*, "Large, non-saturating magnetoresistance in WTe₂," *Nature*, vol. 514, pp. 205-+, Oct 9 2014.
- [21] N. H. D. Khang, Y. Ueda, and P. N. Hai, "A conductive topological insulator with large spin Hall effect for ultralow power spin-orbit torque switching," *Nat Mater*, vol. 17, pp. 808-813, Sep 2018.
- [22] Q. Shao, H. Wu, Q. Pan, P. Zhang, L. Pan, K. Wong, *et al.*, "Room Temperature Highly Efficient Topological Insulator/Mo/CoFeB Spin-Orbit Torque Memory with Perpendicular Magnetic Anisotropy," in *2018 IEEE International Electron Devices Meeting (IEDM)*, 2018, pp. 36.3.1-36.3.4.
- [23] S. Shi, S. Liang, Z. Zhu, K. Cai, S. D. Pollard, Y. Wang, *et al.*, "All-electric magnetization switching and Dzyaloshinskii-Moriya interaction in WTe₂/ferromagnet heterostructures," *Nat Nanotechnol*, vol. 14, pp. 945-949, Oct 2019.
- [24] P. Li, W. K. Wu, Y. Wen, C. H. Zhang, J. W. Zhang, S. F. Zhang, *et al.*, "Spin-momentum locking and spin-orbit torques in magnetic nano-heterojunctions composed of Weyl semimetal WTe₂," *Nature Communications*, vol. 9, Sep 28 2018.
- [25] D. MacNeill, G. M. Stiehl, M. H. D. Guimaraes, R. A. Buhrman, J. Park, and D. C. Ralph, "Control of spin-orbit torques through crystal symmetry in WTe₂/ferromagnet bilayers," *Nature Physics*, vol. 13, p. 300, 11/07/online 2016.
- [26] Y. Fan, P. Upadhyaya, X. Kou, M. Lang, S. Takei, Z. Wang, *et al.*, "Magnetization switching through giant spin-orbit torque in a magnetically doped topological insulator heterostructure," *Nat Mater*, vol. 13, pp. 699-704, Jul 2014.
- [27] R. Ramaswamy, T. Dutta, S. Liang, G. Yang, M. S. M. Saifullah, and H. Yang, "Spin orbit torque driven magnetization switching with sputtered Bi₂Se₃ spin current source," *Journal of Physics D: Applied Physics*, vol. 52, p. 224001, 2019/03/21 2019.
- [28] P. Corbae, S. Ciocys, D. Varjas, S. Zeltmann, C. H. Stansbury, M. Molina-Ruiz, *et al.*, "Evidence for topological surface states in amorphous Bi₂Se₃," *arXiv preprint arXiv:1910.13412*, 2019.
- [29] Y.-B. Yang, T. Qin, D.-L. Deng, L. M. Duan, and Y. Xu, "Topological Amorphous Metals," *Physical Review Letters*, vol. 123, p. 076401, 08/12/ 2019.
- [30] Y. C. Jiang, J. Gao, and L. Wang, "Raman fingerprint for semi-metal WTe₂ evolving from bulk to monolayer," *Scientific Reports*, vol. 6, p. 19624, 01/22/online 2016.
- [31] F. Ye, J. Lee, J. Hu, Z. Mao, J. Wei, and P. X.-L. Feng, "Environmental Instability and Degradation of Single- and Few-Layer WTe₂ Nanosheets in Ambient Conditions," *Small*, vol. 12, pp. 5802-5808, 2016.
- [32] K. Chen, Z. Chen, X. Wan, Z. Zheng, F. Xie, W. Chen, *et al.*, "A Simple Method for Synthesis of High-Quality Millimeter-Scale 1T' Transition-Metal Telluride and Near-Field Nanooptical Properties," *Advanced Materials*, vol. 29, p. 1700704, 2017.
- [33] M. J. Mleczko, R. L. Xu, K. Okabe, H.-H. Kuo, I. R. Fisher, H. S. P. Wong, *et al.*, "High Current Density and Low Thermal Conductivity of Atomically Thin Semimetallic WTe₂," *ACS Nano*, vol. 10, pp. 7507-7514, 2016/08/23 2016.
- [34] W. L. Liu, M. L. Chen, X. X. Li, S. Dubey, T. Xiong, Z. M. Dai, *et al.*, "Effect of aging-induced disorder on the quantum transport properties of few-layer WTe₂," *2D Materials*, vol. 4, p. 011011, 2016/12/14 2016.

- [35] S. Hikami, A. I. Larkin, and Y. Nagaoka, "Spin-Orbit Interaction and Magnetoresistance in the Two Dimensional Random System," *Progress of Theoretical Physics*, vol. 63, pp. 707-710, 1980.
- [36] L. Wang, I. Gutiérrez-Lezama, C. Barreteau, N. Ubrig, E. Giannini, and A. F. Morpurgo, "Tuning magnetotransport in a compensated semimetal at the atomic scale," *Nature Communications*, vol. 6, p. 8892, 11/24/online 2015.
- [37] Y. Zhao, H. Liu, J. Yan, W. An, J. Liu, X. Zhang, *et al.*, "Anisotropic magnetotransport and exotic longitudinal linear magnetoresistance in WTe_2 crystals," *Physical Review B*, vol. 92, p. 041104, 07/06/ 2015.
- [38] X.-C. Pan, Y. Pan, J. Jiang, H. Zuo, H. Liu, X. Chen, *et al.*, "Carrier balance and linear magnetoresistance in type-II Weyl semimetal WTe_2 ," *Frontiers of Physics*, vol. 12, p. 127203, June 09 2017.
- [39] Y. Wang, E. Liu, H. Liu, Y. Pan, L. Zhang, J. Zeng, *et al.*, "Gate-tunable negative longitudinal magnetoresistance in the predicted type-II Weyl semimetal WTe_2 ," *Nature Communications*, vol. 7, p. 13142, 2016/10/11 2016.
- [40] P. Li, Y. Wen, X. He, Q. Zhang, C. Xia, Z. M. Yu, *et al.*, "Evidence for topological type-II Weyl semimetal WTe_2 ," *Nature Communications*, vol. 8, Dec 15 2017.
- [41] P. A. Lee and T. V. Ramakrishnan, "Disordered electronic systems," *Reviews of Modern Physics*, vol. 57, pp. 287-337, 04/01/ 1985.
- [42] X. Dai, H.-Z. Lu, S.-Q. Shen, and H. Yao, "Detecting monopole charge in Weyl semimetals via quantum interference transport," *Physical Review B*, vol. 93, p. 161110, 04/18/ 2016.
- [43] B. Zhao, P. Cheng, H. Pan, S. Zhang, B. Wang, G. Wang, *et al.*, "Weak antilocalization in $\mathrm{Cd}_3\mathrm{As}_2$ thin films," *Scientific Reports*, vol. 6, p. 22377, 03/03/online 2016.
- [44] H.-Z. Lu and S.-Q. Shen, "Weak antilocalization and localization in disordered and interacting Weyl semimetals," *Physical Review B*, vol. 92, p. 035203, 07/07/ 2015.
- [45] M. Hirata, K. Ishikawa, G. Matsuno, A. Kobayashi, K. Miyagawa, M. Tamura, *et al.*, "Anomalous spin correlations and excitonic instability of interacting 2D Weyl fermions," *Science*, vol. 358, pp. 1403-1406, 2017.
- [46] J. J. Lin and J. P. Bird, "Recent experimental studies of electron dephasing in metal and semiconductor mesoscopic structures," *Journal of Physics: Condensed Matter*, vol. 14, pp. R501-R596, 2002/04/26 2002.
- [47] L. Liu, O. J. Lee, T. J. Gudmundsen, D. C. Ralph, and R. A. Buhrman, "Current-Induced Switching of Perpendicularly Magnetized Magnetic Layers Using Spin Torque from the Spin Hall Effect," *Physical Review Letters*, vol. 109, p. 096602, 08/29/ 2012.
- [48] J. Zhou, J. Qiao, A. Bournel, and W. Zhao, "Intrinsic spin Hall conductivity of the semimetals MoTe_2 and WTe_2 ," *Physical Review B*, vol. 99, p. 060408, 02/26/ 2019.
- [49] A. Hoffmann, "Spin Hall Effects in Metals," *Ieee Transactions on Magnetism*, vol. 49, pp. 5172-5193, Oct 2013.
- [50] G. Vignale, "Ten Years of Spin Hall Effect," *Journal of Superconductivity and Novel Magnetism*, vol. 23, p. 3, October 01 2009.
- [51] N. Nagaosa, J. Sinova, S. Onoda, A. H. MacDonald, and N. P. Ong, "Anomalous Hall effect," *Reviews of Modern Physics*, vol. 82, pp. 1539-1592, 2010.
- [52] S. Ryu, A. P. Schnyder, A. Furusaki, and A. W. W. Ludwig, "Topological insulators and superconductors: tenfold way and dimensional hierarchy," *New Journal of Physics*, vol. 12, p. 065010, 2010/06/17 2010.
- [53] A. Fert and P. M. Levy, "Spin Hall Effect Induced by Resonant Scattering on Impurities in Metals," *Physical Review Letters*, vol. 106, p. 157208, 04/15/ 2011.

- [54] O. Mosendz, J. E. Pearson, F. Y. Fradin, G. E. W. Bauer, S. D. Bader, and A. Hoffmann, "Quantifying Spin Hall Angles from Spin Pumping: Experiments and Theory," *Physical Review Letters*, vol. 104, 2010.
- [55] T. Liu, Y. Zhang, J. W. Cai, and H. Y. Pan, "Thermally robust Mo/CoFeB/MgO trilayers with strong perpendicular magnetic anisotropy," *Sci Rep*, vol. 4, p. 5895, Jul 31 2014.
- [56] M. Hayashi, J. Kim, M. Yamanouchi, and H. Ohno, "Quantitative characterization of the spin-orbit torque using harmonic Hall voltage measurements," *Physical Review B*, vol. 89, p. 144425, 04/29/ 2014.
- [57] C. O. Avci, K. Garello, M. Gabureac, A. Ghosh, A. Fuhrer, S. F. Alvarado, *et al.*, "Interplay of spin-orbit torque and thermoelectric effects in ferromagnet/normal-metal bilayers," *Physical Review B*, vol. 90, p. 224427, 12/31/ 2014.
- [58] C. O. Avci, K. Garello, A. Ghosh, M. Gabureac, S. F. Alvarado, and P. Gambardella, "Unidirectional spin Hall magnetoresistance in ferromagnet/normal metal bilayers," *Nature Physics*, vol. 11, p. 570, 06/08/online 2015.
- [59] K. Yasuda, A. Tsukazaki, R. Yoshimi, K. S. Takahashi, M. Kawasaki, and Y. Tokura, "Large Unidirectional Magnetoresistance in a Magnetic Topological Insulator," *Physical Review Letters*, vol. 117, p. 127202, 09/14/ 2016.
- [60] S. Langenfeld, V. Tshitoyan, Z. Fang, A. Wells, T. A. Moore, and A. J. Ferguson, "Exchange magnon induced resistance asymmetry in permalloy spin-Hall oscillators," *Applied Physics Letters*, vol. 108, p. 192402, 2016.
- [61] C. O. Avci, J. Mendil, G. S. D. Beach, and P. Gambardella, "Origins of the Unidirectional Spin Hall Magnetoresistance in Metallic Bilayers," *Physical Review Letters*, vol. 121, p. 087207, 08/24/ 2018.
- [62] Y. Cheng, K. Chen, and S. Zhang, "Interplay of magnon and electron currents in magnetic heterostructure," *Physical Review B*, vol. 96, p. 024449, 07/31/ 2017.
- [63] S. S. L. Zhang and G. Vignale, "Theory of unidirectional spin Hall magnetoresistance in heavy-metal/ferromagnetic-metal bilayers," *Physical Review B*, vol. 94, p. 140411, 10/17/ 2016.
- [64] K. Yasuda, A. Tsukazaki, R. Yoshimi, K. Kondou, K. S. Takahashi, Y. Otani, *et al.*, "Current-Nonlinear Hall Effect and Spin-Orbit Torque Magnetization Switching in a Magnetic Topological Insulator," *Physical Review Letters*, vol. 119, Sep 28 2017.
- [65] Z. Chi, Y.-C. Lau, X. Xu, T. Ohkubo, K. Hono, and M. Hayashi, "The spin Hall effect of Bi-Sb alloys driven by thermally excited Dirac-like electrons," *arXiv preprint arXiv:1910.12433*, 2019.
- [66] A. Agarwala and V. B. Shenoy, "Topological Insulators in Amorphous Systems," *Physical Review Letters*, vol. 118, p. 236402, 06/08/ 2017.
- [67] A. Banerjee, O. Deb, K. Majhi, R. Ganesan, D. Sen, and P. S. Anil Kumar, "Granular topological insulators," *Nanoscale*, vol. 9, pp. 6755-6764, 2017.